JMEPEG (2021) 30:7223–7235
https://doi.org/10.1007/s11665-021-05907-w

1059-9495/$19.00

Microstructure and Magnetron Sputtering Properties of W/Re Alloy Targets Fabricated by Vacuum Sintering

Y.M. Wang, Q.H. Tang, and P. Zhou

Submitted: 15 January 2021 / Revised: 5 May 2021 / Accepted: 6 May 2021 / Published online: 2 June 2021

To develop high-quality refractory metal targets, pure W and W/Re alloys (with Re contents of 1, 5 and 10 mass%) were fabricated via mechanical mixing, press forming and vacuum sintering. Properties such as relative density, grain size and orientation, and magnetron sputtering characteristics were investigated in the W/Re alloys. With increasing Re content, both the relative density and purity of the W-Re alloys increased, while the grain size decreased. The sizes of the grains in the W/10 mass% Re alloy target were mainly between 10 and 40 μm. The results of electron backscatter diffraction (EBSD) indicated that the grains in the W/Re alloys were randomly distributed and did not have a preferred orientation. The percentage of small-angle grain boundaries (< 10°) was greater than 85% in the W/10 mass% Re alloy. The grains in W/Re alloy thin films became gradually refined with increasing deposition pressure during magnetron sputtering. Additionally, the surface roughness of the thin films gradually decreased and the thickness of the thin films gradually increased with increasing deposition pressure. X-ray diffraction (XRD) patterns of the thin films exhibited (110), (200) and (211) diffraction peaks at 40.5°, 58.6° and 73.5°, respectively. With increasing deposition pressure, the intensity of the (110) diffraction peak gradually decreased, while the intensity of the (200) diffraction peak gradually increased.

Keywords magnetron sputtering properties, thin film, vacuum sintering, W/Re alloy target

1. Introduction

Tungsten (W) is a unique element with a high melting point, excellent conductivity, high electromigration resistance, a work function close to the band gap of silicon and excellent thermal stability; additionally, it bonds extremely well with silicon. As a result, high-purity tungsten and tungsten alloys can be used as gate circuit materials, wiring materials and shielding materials for large-scale integrated circuits (Ref 1). In recent years, high-purity tungsten and tungsten alloy (W-Ti, W-Si, etc.) targets have been developed and widely used in the semiconductor industry to manufacture large-scale integrated circuits (Ref 2-12).

The density and purity of these targets as well as grain size and grain size distribution, grain orientation and texture were found to be the main factors influencing target performance during sputtered deposition (Ref 13,14). Taking the grain size and grain size distribution as examples, the sputtering rate for a fine-grained target was faster than that for a coarse-grained target. The thickness of deposited thin films was more uniform when the target had a smaller grain size distribution. In addition, additive elements such as Re, Mo, Ta and Ti have been shown to have a large influence on the grain size distribution in tungsten matrices (Ref 15). For example, the atomic radii, densities and melting points of Re and W are nearly identical owing to their similar atomic numbers. When the recrystallization temperature of Re is 500 °C higher than that of W, the recrystallization temperature of W/Re alloys can be increased by the addition of Re. Tungsten grains can be significantly refined by Re. As a result, Re is a preferred additive element for tungsten alloy targets.

W/Re alloys with high purities and densities can be used as target materials for magnetron sputtering in the semiconductor industry. For example, a W/Re alloy can be used as a diffusion barrier between silicon and aluminum in semiconductor materials (Ref 16, 17), as these alloys are inert in the presence of silicon and aluminum. Moreover, W-Re alloys can replace copper as a semiconductor interconnect material. At temperatures higher than 200 °C, W-Re alloys can be used as functional contact layers due to their chemical inertness, which can reduce the aging of interconnects and other related materials (Ref 18, 19). With improvements in semiconductor integration and decreases in wiring size, stricter requirements regarding the purity, density and filling performance of wiring materials have been enacted. As a result, W/Re alloy sputtering targets with ultrahigh purities and densities will become indispensable raw materials for the continued development of semiconductor nanotechnologies.

The processing of W/Re alloys has played an increasingly important role in the microelectronics industry (Ref 20-24). The main processing techniques used to fabricate W/Re alloys include melt casting, chemical vapor deposition, plasma spray and powder metallurgy. The creep behavior of arc-melted W-3.6 mass% Re-0.33 mass% ZrC and W-5.0 mass% Re, which were considered as potential emitters for a thermionic energy converter, was evaluated at elevated temperatures (1900-2400K) under stresses of 15-80 MPa and vacuum pressures below 1.3×10^{-6} Pa (1.0×10^{-8} torr) (Ref 25). The recrystal-

Y.M. Wang, Q.H. Tang, and **P. Zhou**, Hunan Provincial Key Defense Laboratory of High Temperature Wear-Resisting Materials and Preparation Technology, Hunan University of Science and Technology, Xiangtan 411201, China; and Hunan Provincial Key Laboratory of Advanced Materials for New Energy Storage and Conversion, Hunan University of Science and Technology, Xiangtan 411201, China. Contact e-mail: wym_@163.com.

lization temperature of a W/Re alloy prepared by chemical vapor deposition was 300-500 °C higher than that of pure W, which was attributed to the addition of 3-5 mass% Re (Ref 26). A W-5.0 mass% Re composite feedstock was fabricated by a new cover method, and complex and thin-walled W-5.0 mass% Re products were produced by plasma spray forming (PSF) followed by hot isostatic pressing (HIPing) (Ref 27, 28). Pure W and W-3.5 mass% Re alloys were fabricated by high-energy ball milling followed by spark plasma sintering (Ref 29). Pure W was not able to completely densify (relative density of approximately 93%) at a sintering temperature of 1500 °C in this work. However, the addition of 5 mass% Re resulted in nearly complete densification (relative density of nearly 97%) at the same sintering temperature. The enhanced densification of the W-Re powders was mainly attributed to the ductility of Re, the nanocrystallinity of the powders and the application of pressure during sintering.

However, for almost all available references, research has been mainly focused on the radiation–precipitation mechanism and the thermal potential of W/Re alloys. There is still a lack of research investigating the microstructure and magnetron sputtering properties of W/Re alloy targets. Thus, the objective of the current work was to systematically study the composition of raw materials and the density, microarea composition, grain size and grain size distribution, and grain orientation distribution in vacuum-sintered W-Re alloy targets. The microstructures and phases observed in thin films that were magnetron-sputtered from a W/10 mass% Re alloy target were compared.

2. Experimental Procedure

Tungsten and rhenium raw powders were purchased from Zhuzhou Cemented Carbide Group Co., Ltd. and Beijing Xingrongyuan Technology Co., Ltd., respectively. The tungsten particles were small, polygonal in shape and substantially agglomerated, as shown in Fig. 1(a). The average particle size (see Fig. 1b) and purity of the initial tungsten powders were approximately 8.5 μm and 99.95 mass%, respectively. The initial rhenium particles were irregular and overlapped with one other, as shown in Fig. 1(c). The average particle size (see Fig. 1d) and purity of the rhenium powders were approximately 31.0 μm and 99.90 mass%, respectively. The particle size distribution in the raw powders was measured with a laser particle size analyzer (Mastersizer Micro-Plus, Malvern Panalytical). The composition of the raw powders, which were provided by the above-mentioned manufacturers, is shown in Table 1.

Three W/Re composite powders with different Re contents (1 mass%, 5 mass% and 10 mass%) were prepared in a horizontal mixer (XQM-8L, Nanjing Scientific Analysis Experimental Instrument Research Institute Co., Ltd.) with a mixing time of 6 h. The composite powders were press-molded with a Y41-20T four-column hydraulic machine under a pressure of 10 MPa for 15 s. Then, the pressed, rough billets were placed in a GJJ-23-250-2.5-type vacuum sintering furnace. First, the sintering furnace was allowed to reach a vacuum pressure of 300 Pa (accuracy of ± 10 Pa). Second, the vacuum furnace was heated to 850 °C at a rate of 3 °C min^{-1}, and the pressed, rough billets were held at 850 °C for 150 min. Third, the vacuum furnace was heated to 2250 °C at a rate of 2 °C min^{-1}, and the composite samples were held at 2250 °C (accuracy of ± 5 °C) for 420 min. Fourth, the composite samples were cooled to 23 °C at a rate of 2 °C min^{-1}, and the furnace was filled with protective nitrogen gas. Finally, the samples were removed from the furnace.

After vacuum sintering, the samples were ground and polished to the designed dimensions. Magnetron sputtering (JGP450, Sky Technology Development Co. Ltd., China) was then performed according to the following steps. (1) Monocrystalline silicon substrates were first ultrasonically cleaned with petroleum ether for 20 min and then washed with deionized water for 10 min. The substrates were further cleaned with absolute ethyl alcohol and dried with a hair dryer. (2) The substrates were placed on a heating table in the sputtering chamber. (3) The pressure of the sputtering chamber reached 5.0×10^{-4} Pa (accuracy of $\pm 0.5 \times 10^{-4}$ Pa) after it was evacuated four times. (4) The samples were heated to 200 °C (accuracy of ± 5 °C) at 8 °C min^{-1}. (5) High-purity argon gas was introduced into the sputtering chamber at a rate of 3.33×10^{-4} m^3 s^{-1} using a flowmeter. (6) The pressure of the sputtering chamber was kept stable with adjustments. (7) Thin films were allowed to grow by turning the DC power on. (8) Finally, the thin film samples were removed from the vacuum chamber after it was cooled to 100 °C. The magnetron sputtering parameters are provided in Table 2. It should be noted that only one parameter, the working pressure, is discussed in this paper. All of the other parameters, including the Ar flow rate, base pressure, DC power, sample rotating speed, heating temperature and sputtering time, were kept constant.

The densities of pure W and the W/Re alloy targets were measured using Archimedes' principle (accuracy of ± 2%). Relative densities are reported herein. The phase constituents of the W/Re composite powders, vacuum-sintered W/Re alloys and magnetron-sputtered W/Re thin films were identified using an x-ray diffractometer with 40 kV and 300 mA CuKa radiation (D/ruax2550, Rigaku). Samples for metallographic study were ground with emery papers and mechanically polished with 4-8 and 0.5-1 μm diamond pastes. The samples were all etched with a unique, corrosive solution (ammonia in water and hydrogen peroxide at a volume ratio of 1:2) for 30 s and then characterized by metallurgical microscopy (Leica DM2700, Leica Camera AG). Scanning electron microscopy (SEM) (Quanta FEG 250 and Nova Nanosem 230, FEI) was used to characterize the surfaces and fracture surfaces of the W/Re composite powders, vacuum-sintered W/Re alloys and magnetron-sputtered W/Re thin films. Elemental maps of the W/Re alloy target were obtained with a field emission electron probe microanalyzer (JXA-8230F, JEOL). EBSD (Helios NanoLab G3 UC, FEI) analysis was also performed to examine the crystallographic orientation of grains in the vacuum-sintered W/Re alloys. For EBSD analysis, samples were polished using 0.5-1 μm diamond pastes and then vibratory polished for 360 min with a vibratory polishing machine (ZPG-300, Shanghai Metallurgical Equipment Co., Ltd.). EBSD images were taken at a magnification of 20000 × with a step size of 0.03 μm. During image postprocessing, with the aid of TSL OIM Analysis 5 software, data points with a confidence index lower than 0.05 were removed. No other cleanups were applied to the datasets.

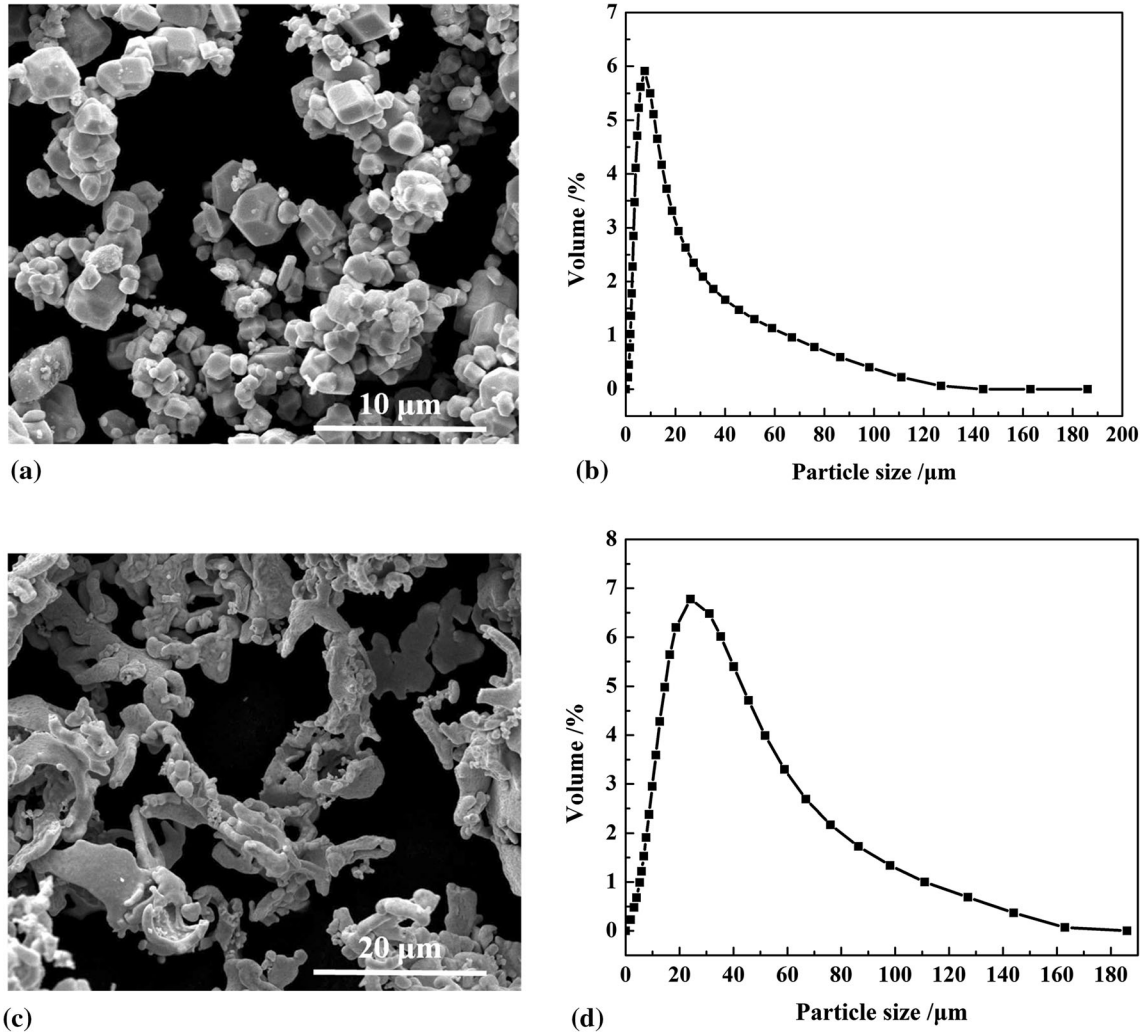

Fig. 1 Tungsten and rhenium powders. (a) SEM image of and (b) laser particle size distribution in the tungsten powder. (c) SEM image of and (d) laser particle size distribution in the rhenium powder

Table 1 Composition of the raw powders

Raw materials	Fe, mass%	Ca, mass%	Si, mass%	O, mass%	Mo, mass%	Al, mass%	P, mass%	C, mass%	Na, mass%
W	0.0005	0.0005	0.0005	0.0010	0.0005	0.0005	0.0005	0.0010	…
Re	0.0010	0.0010	0.0015	0.0015	0.0010	0.0010	0.0010	0.0015	0.0005

Table 2 Magnetron sputtering parameters for the W/Re alloy targets

Sample No.	Ar flow rate, L h^{-1}	Working pressure, Pa	Base pressure, Pa	DC powder, W	Sample rotating speed, rpm	Heating temperature, °C	Sputtering time, min	Target materials
1	50	0.20	6.0×10^{-4}	30	10	300	60	W-10 mass% Re
2	50	0.30	6.0×10^{-4}	30	10	300	60	W-10 mass% Re
3	50	0.40	6.0×10^{-4}	30	10	300	60	W-10 mass% Re
4	50	0.50	6.0×10^{-4}	30	10	300	60	W-10 mass% Re

3. Results and Discussion

3.1 Morphology and Phase Constitution of the W/Re Composite Powders

After mechanical mixing, the W/Re composite powders were substantially agglomerated, as shown in Fig. 2(a-c). Moreover, the number of flake-like particles in the W/Re composite powders increased with increasing Re content (see Fig. 2). The fine W powder adhered to the surface of the flake-like Re particles, as shown in Fig. 2(c). For the W/Re composite powders containing 1 mass% Re, 5 mass% Re and 10 mass% Re, the average particle size (see Fig. 2d) was 14.6 μm, 15.1 μm and 16.2 μm, respectively. It can be concluded that the average particle size of the W/Re composite powders gradually increased with the amount of the coarse Re powder added.

Major W diffraction peaks and minor Re diffraction peaks can be seen in the XRD pattern presented in Fig. 3. It should be noted that the Re powder was evenly distributed on the W particles after mechanical mixing, and no alloying occurred

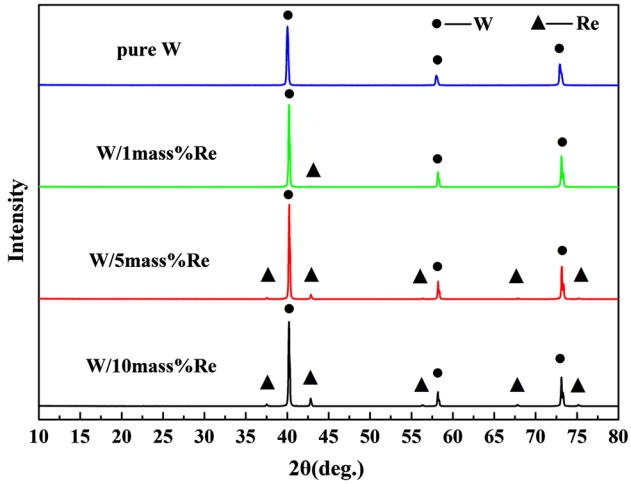

Fig. 3 XRD patterns of the pure W powder and the mixed W/Re powders

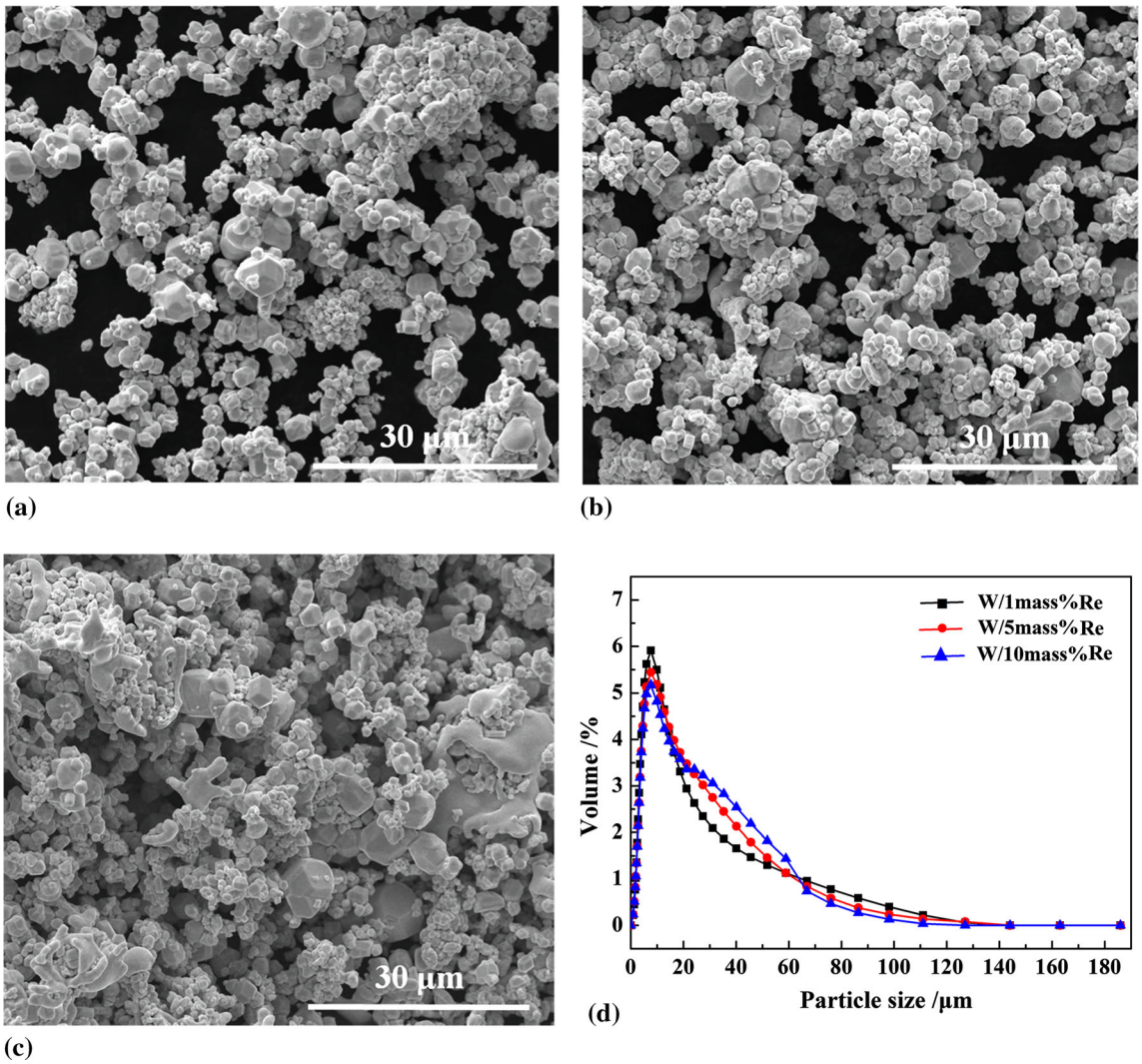

Fig. 2 SEM image of and laser particle size distribution in the W/Re powders: (a) W/1mass% Re, (b) W/5 mass% Re, (c) W/10 mass% Re. (d) Laser particle size distribution

between them. The W diffraction peak positions observed in the W/1 mass% Re, W/5 mass% Re and W/10 mass% Re composite powders are slightly higher than those observed in the pure W powder (see Fig. 3), which may be due to residual stresses caused by mechanical mixing. It should be noted that there is no obvious difference among the W peak positions observed in the above-mentioned composite powders (W/1 mass% Re, W/5 mass% Re and W/10 mass% Re).

3.2 Morphology and Phase Constitution of the Vacuum-Sintered W/Re Alloys

Micropores are observed in pure W and the W/Re alloys fabricated by vacuum sintering, as shown in Fig. 4. In addition, the number of micropores gradually decreases with increasing Re content. The relative densities of vacuum-sintered W and the vacuum-sintered W/1 mass% Re, W/5 mass% Re and W/10 mass% Re alloys are 90.4%, 92.4%, 94.7% and 97.8%, respectively. The density of the W/Re alloys increased gradually with increasing Re content because Re plays an important role in enhancing the density of alloys (Ref 29). It should be noted that both the target erosion rate and the thin film deposition rate increased with the density of the target during magnetron sputtering (Ref 30).

Metallographic images of vacuum-sintered, pure W and the vacuum-sintered W/Re alloys after etching are shown in Fig. 5. The gray and white regions in the etched microstructure (see Fig. 5) are attributed to the same W/Re alloy phase but do not separate the W phase and the Re phase. It is worth noting that the different colors observed in Fig. 5 may be caused by different grain heights after corrosion. The grains in pure W and the W/Re alloys are polygonal in shape and have relatively uniform grain sizes (see Fig. 5). There is no significant difference in grain size between pure W and W/1 mass% Re, as shown in Fig. 5(a) and (b), respectively. The grains in the W/5 mass% Re and W/10 mass% Re alloys are obviously refined, as shown in Fig. 5(c) and (d), respectively. It can be concluded that the addition of Re plays an important role in inhibiting grain growth in the W/Re alloys during high-temperature vacuum sintering owing to 'Re effects' (Ref 31-33). The deposition rate for a target with a small grain size was found to be higher than that for the same target with a large grain size (Ref 34). Furthermore, the quality of the thin film deposited from the former was higher than that deposited from the latter. As such, the addition of Re can help to improve the W target sputtering deposition rate and the quality of corresponding thin films.

Only diffraction peaks attributed to W can be seen in the XRD patterns of the vacuum-sintered W/Re alloys (see Fig. 6) and are consistent with those of pure tungsten. These results indicate that elemental diffusion occurred during high-temperature vacuum sintering and that Re completely dissolved in the W matrix. In contrast to the diffraction peaks of the W/Re mixed powders (see Fig. 3), Re diffraction peaks were absent in the vacuum-sintered W/Re alloys, as shown in Fig. 6.

Figure 7(b_1-b_4), (c_2-c_4) and (d_1-d_4) presents elemental maps of W, Re and O in the investigated areas of pure W and the W/

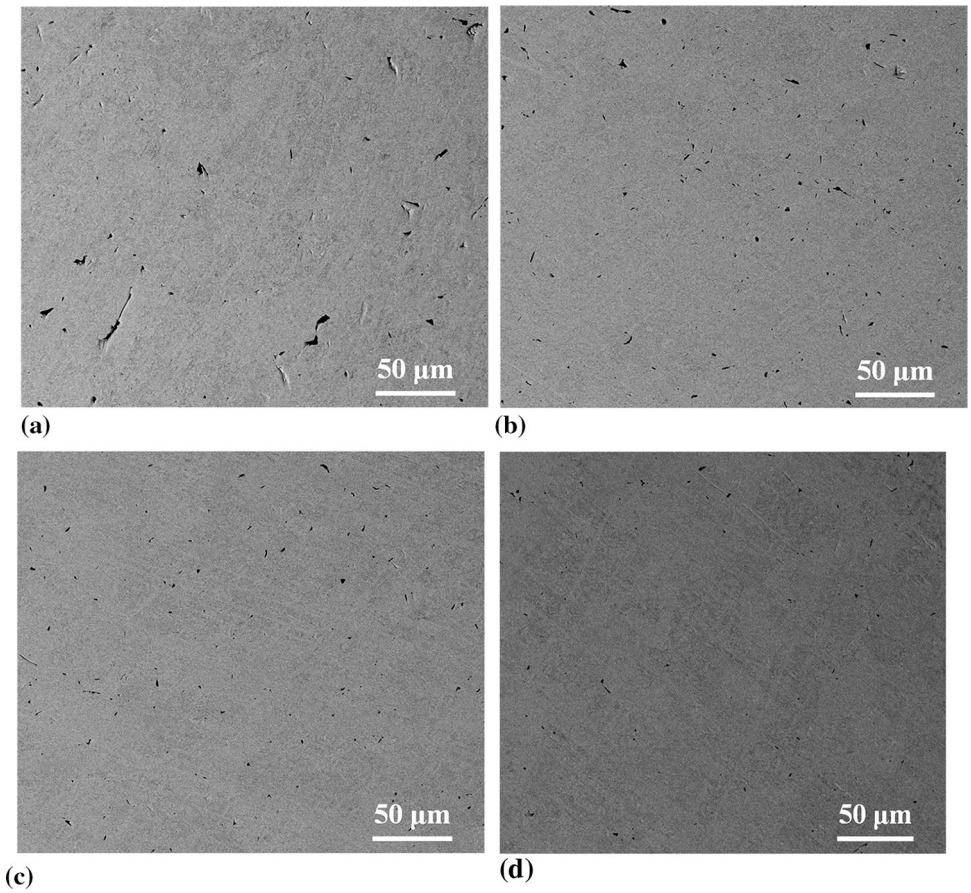

Fig. 4 SEM image of pure W and the W/Re alloys fabricated by vacuum sintering: (a) pure W, (b) W/1 mass% Re, (c) W/5 mass% Re, (d) W/10 mass% Re

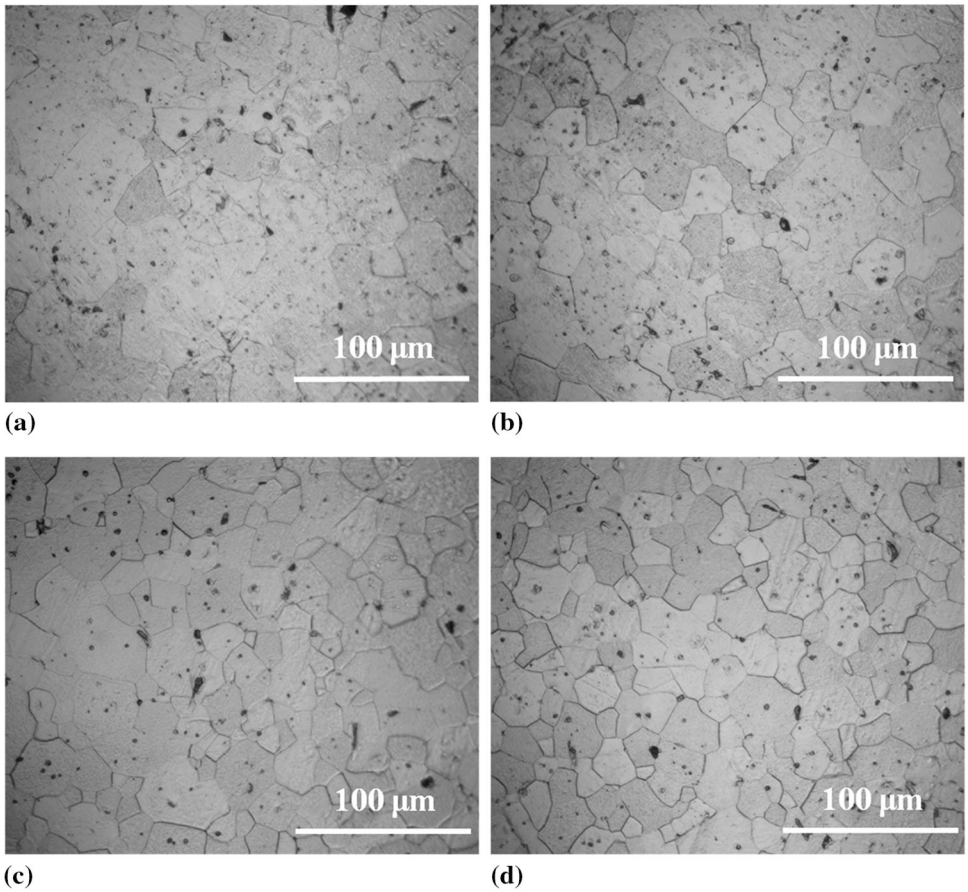

Fig. 5 Images of vacuum-sintered W and the vacuum-sintered W/Re alloys after etching: (a) pure W, (b) W/1 mass% Re, (c) W/5 mass% Re, (d) W/10 mass% Re

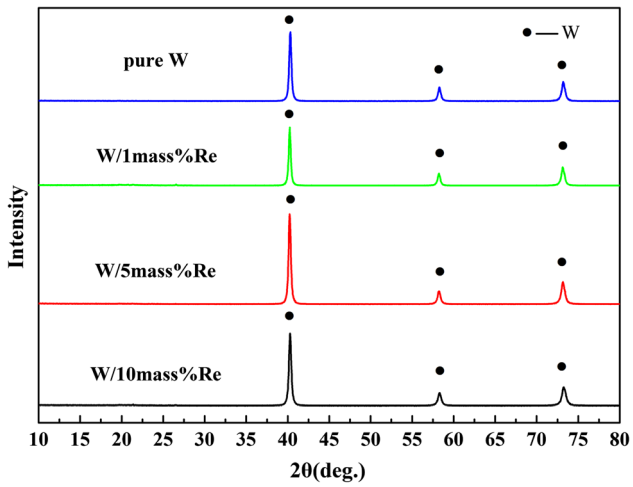

Fig. 6 XRD patterns of pure W and the W/Re alloys prepared by vacuum sintering

Re alloy targets. It should be noted that the Re map of the pure W target, which should be marked as Fig. 7(c_1), is missing in this work. In addition, the concentration of the elements presented in Fig. 7 can be distinguished by the level of color. The deeper the color is, the higher the corresponding element concentration. The color in each region of the investigated area (see Fig. 7) is similar, which indicates that W and Re are evenly distributed in the sample within a single phase. With increasing Re content, the color corresponding to W gradually lightens, while that corresponding to Re gradually deepens. These results are consistent with the variations in the composition of the vacuum-sintered W/Re alloys.

Importantly, the structural uniformity of pure W and W/Re alloy targets has a large influence on the quality of the corresponding sputtered thin films. The uniform composition of pure W and W/Re alloy targets prepared by vacuum sintering can improve the uniformity of magnetron-sputtered thin films. The elemental O maps for pure W and the W/Re alloy targets are shown in Fig. 7(d_1-d_4). The amount of O in the W/Re alloy targets was lower than that in the pure W target. The sputtered thin films were contaminated by impurities from the target and oxygen and moisture in the micropores (Ref 35, 36). To improve the performance of these sputtered thin films, it is necessary to reduce the impurity content in the targets. The amount of O in the W/Re alloy targets decreased with increasing Re content. This indicates that the oxidation resistance of W targets can be improved by the addition of Re because valence electrons from the latter are transferred to the former (Ref 37). As a result, the solubility of O in W/Re alloys can be reduced under the combined actions of a vacuum sintering environment and Re addition. This is in line with the idea that the quality of magnetron-sputtered thin films is dependent on the purity of the target.

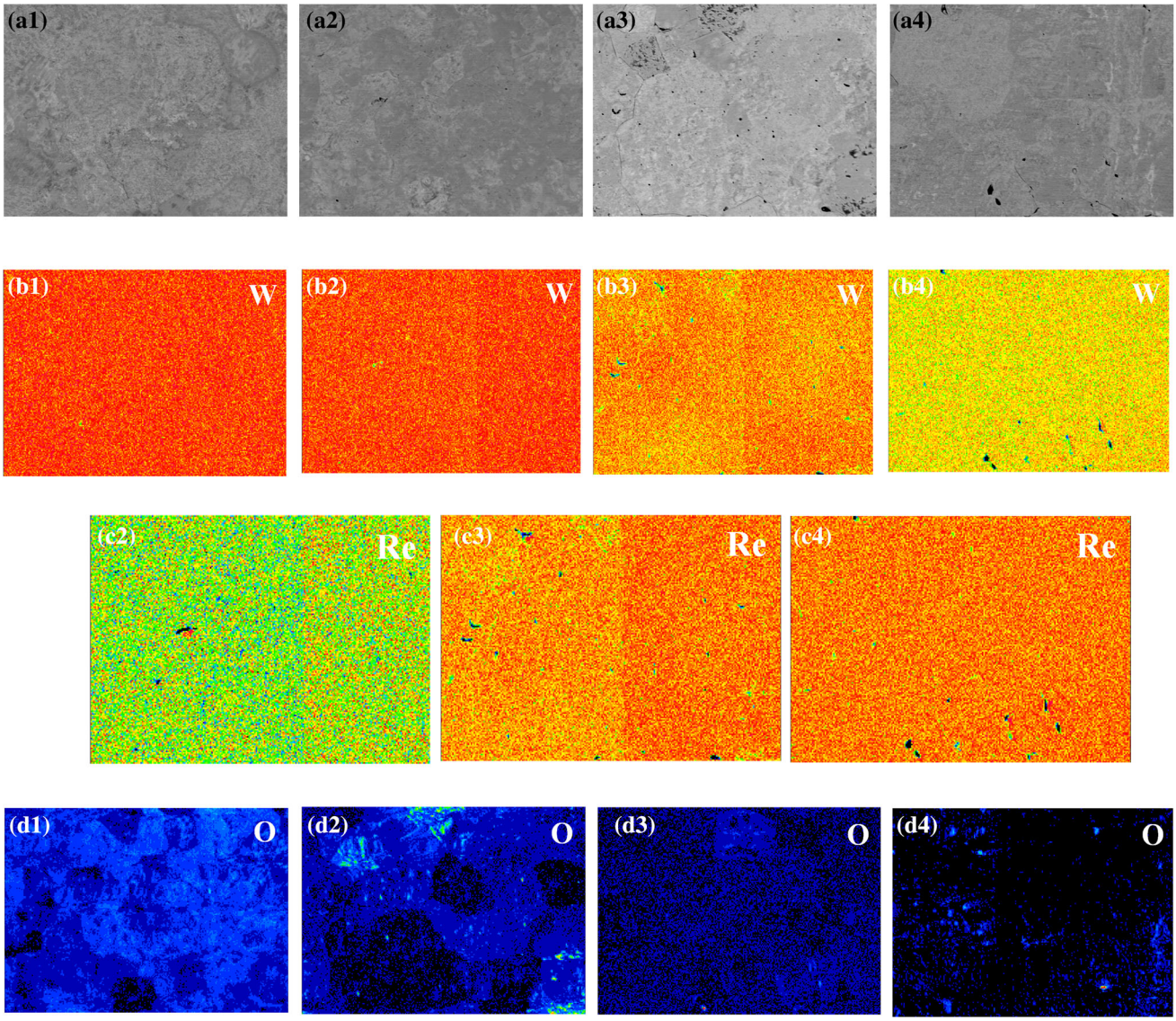

Fig. 7 Elemental maps for pure W and the W/Re alloys obtained with an electron probe microanalyzer. Pure W target: (a_1) image of the investigated area and elemental (b_1) W and (d_1) O maps. W/1 mass% Re target: (a_2) image of the investigated area and elemental (b_2) W (c_2) Re and (d_2) O maps. W/5 mass% Re target: (a_3) image of the investigated area and elemental (b_3) W, (c_3) Re and (d_3) O maps. W/10 mass% Re target: (a_4) image of the investigated area and elemental (b_4) W, (c_4) Re and (d_4) O maps

3.3 Grain Morphology and Orientation in the Vacuum-Sintered W/10 Mass% Re Alloy Target

The morphology of the grains in the vacuum-sintered W/10 mass% Re alloy were examined by EBSD (Fig. 8). The grains in the compact W/10 mass% Re alloy target were fine, equiaxed and had an irregular, polygonal shape (see Fig. 8).

The area fraction of grains with <001>, <011> and <111> orientations in the W/10 mass% Re alloy target was calculated, as shown in Fig. 9. The area fractions of grains with <001>, <011> and <111> orientations were 12.1%, 21.2% and 12.7%, respectively. It has been shown that the more random the grain orientation is, the better the sputtering rate and the uniformity of the sputtered thin film (Ref 38). Hence, the vacuum-sintered W/10 mass% Re alloy, which does not have a preferred orientation, will be beneficial in subsequent magnetron sputtering.

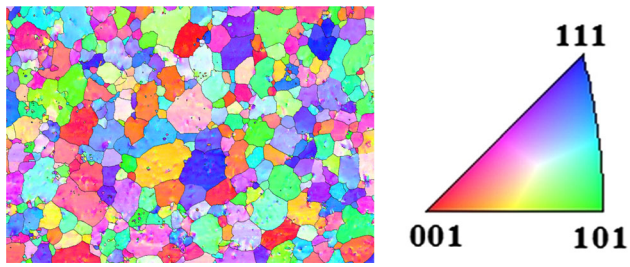

Fig. 8 Large area EBSD map of the W/10 mass% Re alloy target

The pole figure for the vacuum-sintered W/10 mass% Re alloy target is presented in Fig. 10. The projections of all crystal planes, including the (001), (011), (111) and (112) planes, are symmetrically distributed along the RD and TD directions in the W/10 mass% Re alloy. No obvious texture is observed in

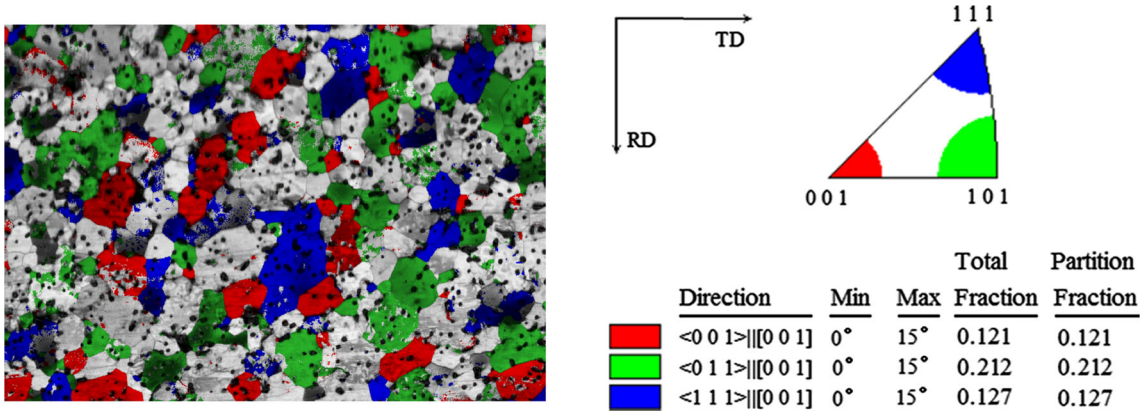

Fig. 9 Distribution and proportion of grains in the W/10 mass% Re target along a given direction

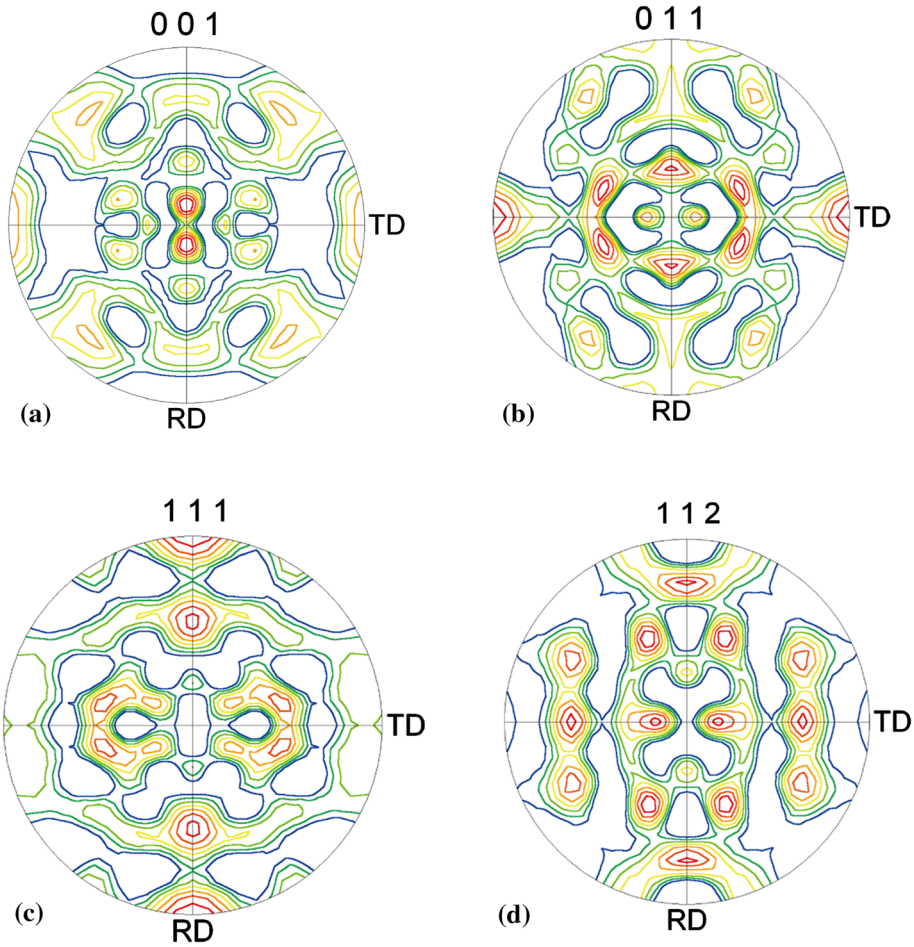

Fig. 10 Pole figure of the vacuum-sintered W/10 mass% Re alloy target: (a) (001) plane, (b) (011) plane, (c) (111) plane and (d) (112) plane

the pole figure because the target was not processed by hot rolling. As a result, the crystal structure of the W/10 mass% Re alloy target is symmetric and uniform and does not have a preferred orientation.

The grain size distribution profile and misorientation angle profile of the grains in the W/10 mass% Re alloy target fabricated by vacuum sintering are shown in Fig. 11(a) and (b), respectively. Most of the grains in the W/10 mass% Re alloy target are between 10 and 40 μm in size and are fine and uniform (see Fig. 11a). Comparing pure W and the W/3 mass% Re and W/5 mass% Re alloys, the smaller grain size of the W/10 mass% Re alloy will allow subsequent magnetron sputtering to be more efficient. The fraction of low-angle grain boundaries ($< 10°$) is greater than 85% (see Fig. 11b).

3.4 Influence of Work Pressure on the Magnetron-Sputtered Thin Films

It can be seen that the W/10 mass% Re alloy target with random grain orientations has the highest density and purity and

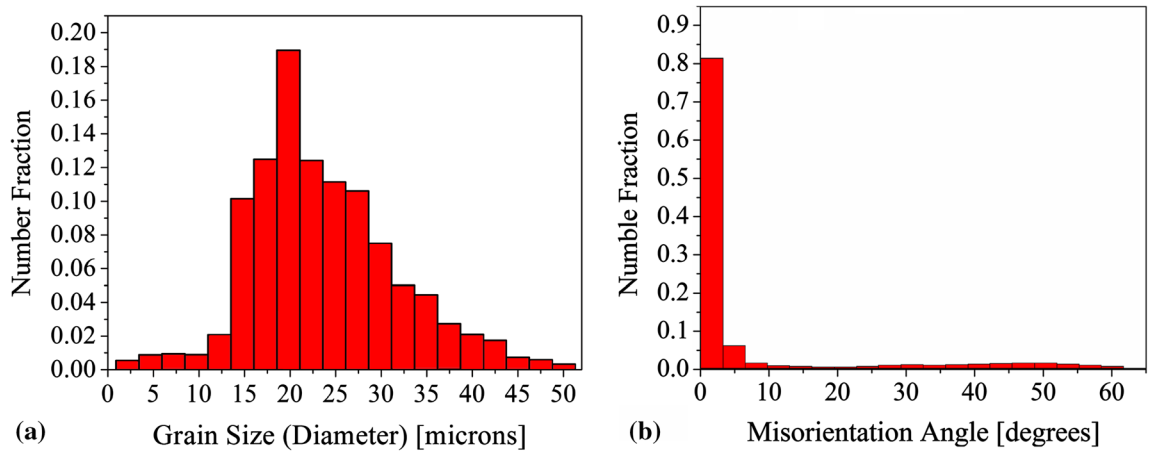

Fig. 11 (a) Grain size distribution profile and (b) misorientation angle profile for the W/10 mass% Re alloy target

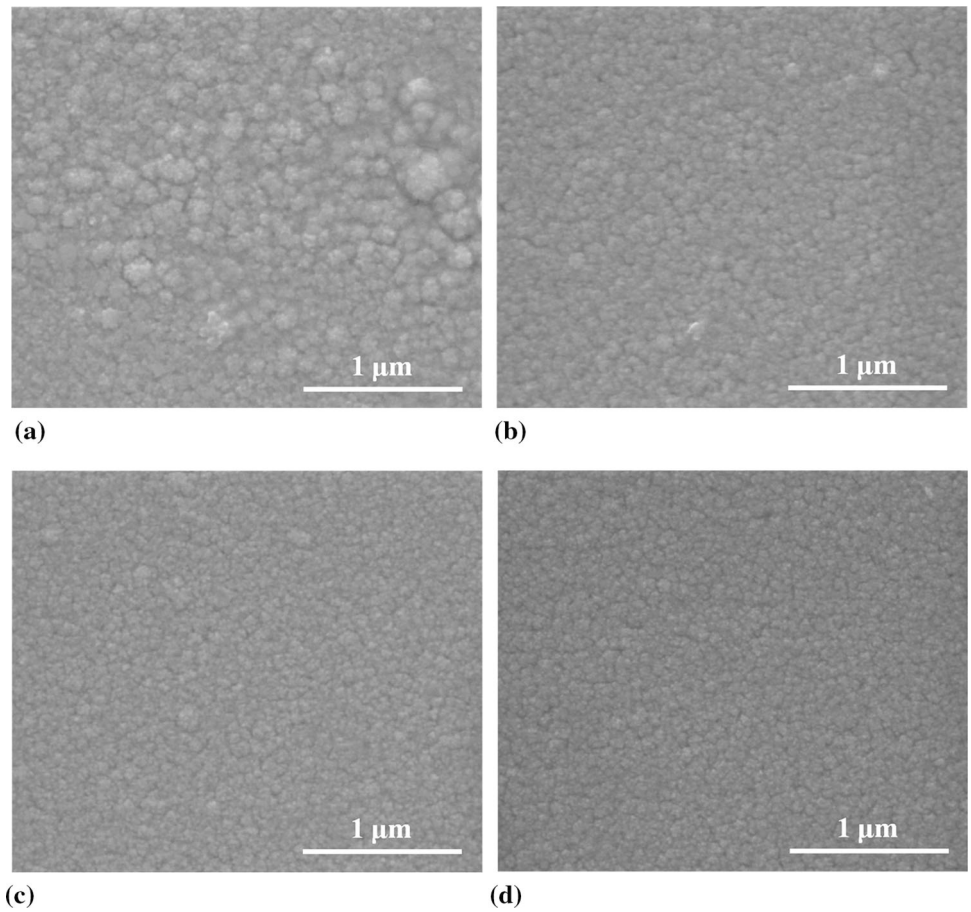

Fig. 12 SEM surface images of the W/Re alloy thin films prepared under different sputtering pressures: (a) 0.2 Pa, (b) 0.3 Pa, (c) 0.4 Pa and (d) 0.5 Pa

the smallest grain size among the four targets from the above-mentioned analyses. The magnetron sputtering properties of the W/10 mass% Re alloy target were thus further investigated.

A smooth, dense and continuous W/Re thin film was deposited on the surface of a monocrystalline silicon substrate by magnetron sputtering of the W/10 mass% Re alloy target. Surface images of the W/Re alloy thin films prepared by magnetron sputtering under different pressures are shown in Fig. 12. Many coarse particles are observed on the surface of the W/Re alloy thin film prepared under a deposition pressure of 0.2 Pa (Fig. 12a). The grains in the W/Re thin films become gradually refined and more uniform (see Fig. 12b-d) as the work pressure increases from 0.2 Pa to 0.3, 0.4 and 0.5 Pa. The surfaces of the W/Re thin films also become more smooth.

Atoms sputtered from the W/Re alloy target collided with other particles (mainly argon atoms) in the deposition chamber

during magnetron sputtering. The energy of the sputtered atoms was reduced before they reached the monocrystalline silicon substrate due to the above-mentioned collisions. Note that the amount of argon in the deposition chamber will increase with increasing work pressure. The energy of sputtered atoms will decrease due to a higher frequency of collisions under higher deposition pressures. These two phenomena resulted in the following. First, the migration ability of the sputtered atoms after they reached the substrate decreased owing to the reduced energy of these atoms. Then, the density of the crystal nuclei increased during film formation. In addition, the size of the grains in the thin film decreased because each crystal nucleus became more refined. Second, the grains in the thin film did not grow completely, and the degree of crystallization was poor owing to the reduced energy of the sputtered atoms. As such, the size of the grains in the thin film was small. Moreover, the surface morphology of the W/Re alloy thin film became more smooth and dense with increasing deposition pressure due to the dense arrangement of crystal nuclei and the small size of the grains.

The thickness of the W/Re alloy thin film prepared under a deposition pressure of 0.2 Pa was only approximately 180.3 nm, as shown in Fig. 13(a). When the deposition pressure was increased to 0.3, 0.4 and 0.5 Pa, the thickness of the W/Re alloy thin film (see Fig. 13b, c and d) gradually increased to 244.8, 273.9 and 313.5 nm, respectively. We expected that the thin film fracture surfaces would be occupied by directionally solidified columnar grains. However, columnar grains could not be clearly identified at the intergranular interfaces due to the small particle size of the grains on the fracture surfaces. Obvious interfaces between the substrate and W/Re thin film were observed at the fracture surfaces, indicating low-element diffusion. Moreover, the thin films adhered well to the substrates, and almost no cracks or pores were observed at the interfaces.

Target atoms can be released by the collision of ions produced from the ionization of argon gas. However, the migration of target atoms can also be hindered by argon gas. It should be noted that the W/Re alloy film fabricated under a pressure of 0.2 Pa was the thinnest of all of the samples investigated (see Fig. 13a). This is attributed to two main events. First, the deposition rate of the W/Re alloy thin film was slow under 0.2 Pa due to a low target sputtering rate. Second, there were fewer collisions between the sputtered particles and

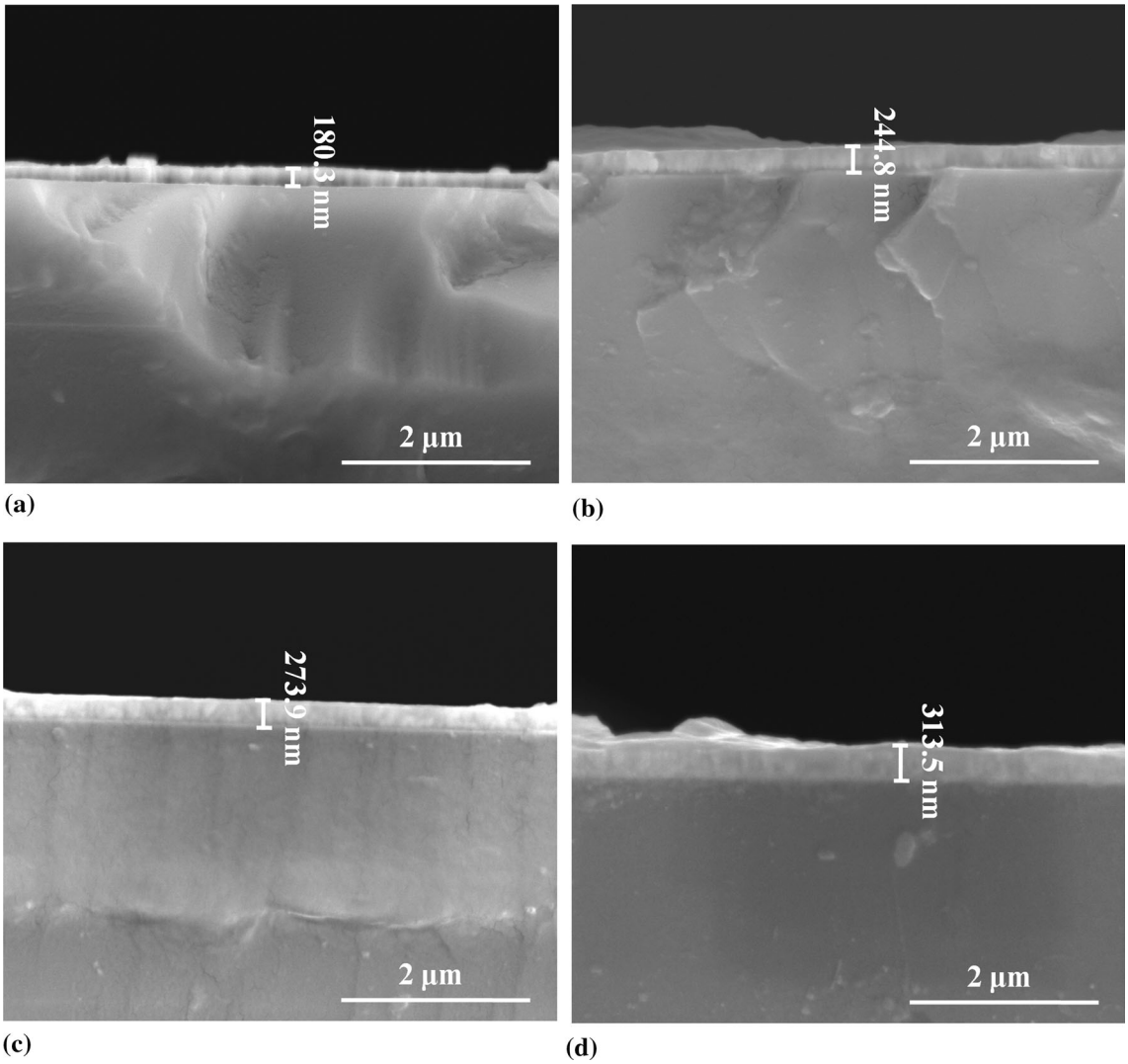

Fig. 13 SEM images of the fracture surfaces of the W/Re alloy thin films prepared under different work pressures: (a) 0.2 Pa, (b) 0.3 Pa, (c) 0.4 Pa and (d) 0.5 Pa

Ar gas during their transport from the target to the substrate under lower working pressures. The sputtered particles were more kinetically energetic during their migration to the monocrystalline silicon substrate. The growth rate and thickness of the W/Re alloy thin film decreased due to a bombardment by resputtered, high-energy particles. This phenomenon is consistent with that reported previously (Ref 39, 40). The number of ions generated by gas ionization increased gradually as the deposition pressure increased to 0.3 Pa and 0.5 Pa. The influence of atoms released by ions impacting the target was greater than that of target atoms hindered by collisions with argon gas. As a result, the thickness of the W/Re alloy thin film increased as the number of target atoms deposited on the monocrystalline silicon substrate increased, as shown in Fig. 13(b-d).

XRD patterns of the W/Re alloy thin films under different sputtering pressures are shown in Fig. 14. Diffraction peaks corresponding to the (110), (200) and (211) crystal planes of α-W are observed at 40.5°, 58.6° and 73.5°, respectively. The W/Re alloy thin films exhibit a unique body-centered cubic structure and contain polycrystalline phases. No impurity diffraction peaks are observed in the XRD patterns. In addition, the intensity of the (110) diffraction peak is much higher than that of the other diffraction peaks, which indicates that the W/Re alloy thin films grew preferentially along the (110) direction during magnetron sputtering. By comparing the peak intensities of the films, it can be seen that the W/Re alloy thin film sputtered under 0.2 Pa possesses the most intense (110) peak; a further increase in the deposition pressure (above 0.2 Pa) yields a less crystalline W/Re alloy thin film, as evidenced by the lower intensity of the (110) diffraction peak. A W/Re alloy film with optimum crystallinity is obtained at the lowest sputtering pressure. This may be caused by the bombardment of highly energetic (kinetic energy) sputtered particles, which results from fewer collisions between W/Re atoms and Ar atoms. Moreover, the intensity of the (200) diffraction peak slightly increases with increasing deposition pressure. At the same time, the grains in the W/Re alloy films become gradually refined and tend to grow along the (200) crystal face.

4. Conclusion

(1) The average particle size of the W/Re mixed powders increased from 14.6 to 16.2 μm as the Re content increased from 1 to 10 mass%. Major W diffraction peaks and minor Re peaks were observed in the XRD patterns because no alloying occurred during mechanical mixing. Compared to the positions of the W diffraction peaks in the pure W powder, the positions of the W diffraction peaks in the W/Re mixed powders (W/1 mass% Re, W/5 mass% Re and W/10 mass% Re) slightly increased, and no obvious differences were observed among the different W/Re mixed powders.

(2) Pure W and W/1 mass% Re, W/5 mass% Re and W/10 mass% Re alloys were prepared by press molding and vacuum sintering. Re was completely dissolved in the W matrix, and a uniform W/Re solid solution was formed during vacuum sintering. The relative densities of the vacuum-sintered W, W/1 mass% Re, W/5 mass%

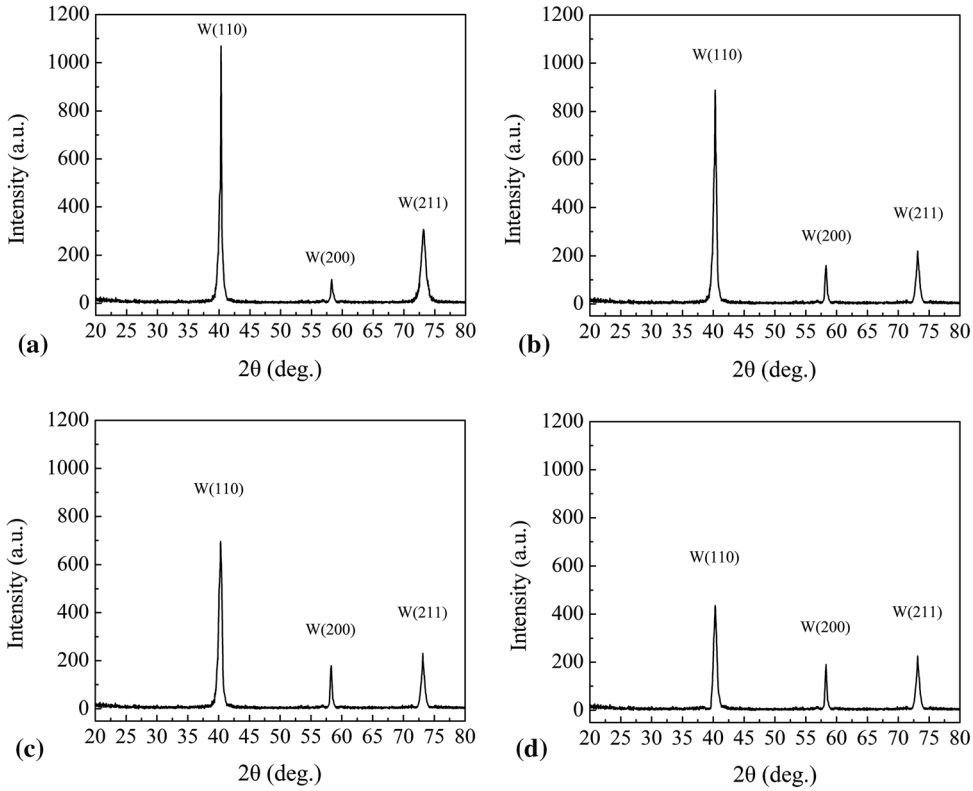

Fig. 14 XRD patterns of the W/Re alloy thin films prepared under different sputtering pressures: (a) 0.2 Pa, (b) 0.3 Pa, (c) 0.4 Pa and (d) 0.5 Pa

Re and W/10 mass% Re samples were 90.4%, 92.4%, 94.7% and 97.8%, respectively. The grains in pure W, W/1 mass% Re, W/5 mass% Re and W/10 mass% Re became more refined with increasing Re content.

(3) The purity of the W/10 mass% Re alloy target was very high, and this sample contained grains with sizes typically between 10 and 40 μm. The percentages of <001>-, <011>- and <111>-oriented grains in the W/10 mass% Re alloy target were 12.1%, 21.2% and 12.7%, respectively. The grains were irregularly distributed and did not have a preferred orientation. In addition, the number fraction of low-angle grain boundaries (< 10°) reached 85%. All of these characteristics can improve the quality of sputtered thin films.

(4) The work pressure has a large influence on the microstructure and properties of W/Re alloy thin films. The grains in the thin films became refined as the deposition pressure increased. At the same time, the coating surface gradually became more smooth and the thickness of the thin film gradually increased. The (110), (200) and (211) diffraction peaks of α-W were observed at 40.5°, 58.6° and 73.5°, respectively. As the deposition pressure increased, the intensity of the (110) diffraction peak decreased gradually, while that of the (200) diffraction peak increased slightly.

Acknowledgments

This work was supported by National Natural Science Foundation of China (Grant No. 51701072 and Grant No. 52011530147), Natural Science Foundation of Hunan Province of China (Grant No. 2016JJ5029, 2017JJ3088 and 2020JJ4738), Military and Civilian Integration Industry Development Special Foundation of Hunan Province (Grant No. 2016B116J1), National United Engineering Laboratory for Advanced Bearing Tribology (Henan University of Science and Technology, Grant No. 201913) and Hunan Province Key Laboratory of Materials Surface & Interface Science and Technology (Central South University of Forestry and Technology, Grant No. KFBJM2019002).

References

1. Y. Yu, J.P. Song, F. Bai, A.L. Zheng and F.S. Peng, Ultra-high Purity Tungsten and Its Applications, *Int. J Refract. Met. Hard Mater.*, 2015, **53**, p 98–103
2. X.Y. Wei, Preparation Technology and Application of High Purity Tungsten Target for Semiconductor, *Cemented Carbide*, 2017, **34**, p 353–359
3. F. Bai, The Study of Preparing of High Purity Tungsten Alloy Targets, A Dissertation Submitted to Xiamen University for Master Degree of Materials Engineering, Xiamen: Xiamen University, 2015, p 40-43
4. Y.Z. Ma, Y. Liu, W.S. Liu and L.P. Long, Preparation Procedure of High Purity Tungsten Via Electron Beam Side Surface Melting, *Mater. Sci. Technol.*, 2014, **22**, p 30–35
5. Z.H. Wang, M.X. Wang, M.Y. Chu, F. Guo, X. Zhao and J.Y. Shen, Preparation of W-Ti Sputtering Targets under Inert Atmosphere, *Chin. J. Rare Met.*, 2006, **30**, p 687–691
6. Z.C. Ding, M. Chen, S.Q. Liu, X.P. Wang and B.G. Lv, Preparation of High Purity W-Si Alloy Powder, *Rare Metal Mat. Eng.*, 2014, **43**, p 1269–1271
7. Z.C. Ding, J.J. He, J.F. Luo, Y.J. Li and X.D. Xiong, Effects of Vacuum Hot Pressing Sintering on the Performance of High Purity W-Si Alloy Target, *Rare Metal Mat. Eng.*, 2014, **43**, p 1403–1406
8. Q.X. Wang and Z.K. Fan, Application and Manufacturing Technology of Tungsten and Tungsten-titanium Targets, *Powder Metall. Technol.*, 2009, **27**, p 52–57
9. Y.M. Wang, Q.H. Tang, D.Q. Chen, X.B. Liu, J.H. Yan and X. Xiong, Microstructure and Magnetron Sputtering Properties of Tungsten Target Fabricated by Low Pressure Plasma Spraying, *Int. J. Refract. Met. Hard Mater.*, 2020, **87**(105116), p 1–10
10. Y.M. Wang, Q.H. Tang, Z.Q. Yan and F. Wang, Influence of Vacuum Chamber Pressure on Microstructure and Properties of Tungsten Target Fabricated by Low Pressure Plasma Spraying, *J. Mater. Eng.*, 2018, **46**, p 104–112
11. B. Gao, L.F. Shao and H.F. Zhang, Preparation and Properties of Metal Tungsten Sputtering Target, *World Nonferr. Met.*, 2017, **33**, p 249–250
12. A.R. Lipski and R.S. Lefferts, Making Tungsten Targets Using Tungsten Oxide Powder, *Nucl. Instrum. Methods Phys. Res. Sect. A*, 2011, **655**, p 41–43
13. Y.Z. Jin, D.L. Liu and J. Chen, Studying on Manufacture and Application of Sputtering Target Materials, *J. Sichuan Univ. Sci. Eng. Nat. Sci. Ed.*, 2005, **18**, p 22–24
14. A.H. Yang, Y. Zhu, Z.M. Deng, H.C. Xie, G.Q. Zhang and F. Wu, Investigation on Microstructure and Texture in High Pure Gold Sputtering Targets by EBSD, *Precious Metal.*, 2014, **35**, p 44–48
15. Y.Q. Xia, D.C. Wang, J.S. Wang, E.K. Zhu and S.L. Yin, Study on High Temperature Molybdenum Alloy Doped with Rare-earth Element, *Chin. Molybden. Indus.*, 2001, **25**, p 76–78
16. S.E. Hornstrom, T. Lin, O. Thomas, P.M. Fryer and J.M.E. Harper, Tungsten-rhenium Alloys as Diffusion Barriers between Aluminum and Silicon, *J. Vacuum Sci. Technol.*, 1988, **6**, p 1650–1655
17. H. Lange, W. Möhling and G. Marxsen, W-Re (6 wt.%) and W-Ti (10 wt.%) Alloys as Diffusion Barriers between Aluminum and Silicon, *Thin Solid Films*, 1991, **205**, p 47-51
18. S.O. Safonov, V.P. Bespalov, A.A. Golishnikov and M.G. Putrya, Estimating the Reliability of Aluminum Metallization of Integrated Circuits by Accelerated Electromigration Testing at Constant Temperature, *Russ. Microelectron.*, 2015, **44**, p 453–459
19. I. De Munari, A. Scorzoni, F. Tamarri and D. Govoni, Drawbacks to Using NIST Electromigration Test-structures to Test Bamboo Metal Lines, *IEEE Trans. Electron Dev.*, 1994, **41**, p 2276–2280
20. T.Y. Cheng, N. Xiong, K.Y. Peng, H.B. Yang and J.C. Yin, The Aplication and Preparation Technology of Rhenium and Rhenium Alloys, *Rare Metal Mat. Eng.*, 2009, **38**, p 373–376
21. H.Z. Wang and S.L. Yang, Character, Application and Preparation Method of Rhenium, *J Chin. Rare Earth Soc.*, 2005, **23**, p 189–193
22. Z.Q. Cui and B.X. Liu, *Metallurgy and Heat Treatment Principle*, Haerbin Institute of Technology Press, Haerbin, 1998
23. J.J. Park, Creep Strength of a Tungsten–rhenium–hafnium Carbide Alloy from 2200 to 2400 , *Mater. Sci. Eng. A*, 1999, **265**, p 174–178
24. K. Yang, B. Cao and W.J. Yu, Precise Resistance Spot Welding of Automotive Lamp, *Electr. Weld. Mach.*, 2010, **40**, p 139–141
25. A. H. Luo, and D. L. Jacobson, Creep Behavior of a Tungsten-3.6%rhenium-0.33%zirconium Carbide Alloy, *Int. J. Refract. Met. Hard Mater.*, 1992, **11**, p 97-103
26. L.Y. Wang, C.Z. Wang, J. Ma and Y.Y. Hou, The Technics of W-Re Alloy Coating by Chemical Vapor Deposition, *China Surf. Eng.*, 2006, **19**, p 39–42
27. Y.M. Wang, M.H. Chen, Y. Li, K.W. Tang, W.W. Ding, X. Xiong, Q.L. Shi, L. Xie and X. Xu, Near-net-shape Tungsten-rhenium Alloy Parts Produced by Shrouded Plasma Spray Forming, *J. Aeronaut. Mater.*, 2016, **36**, p 24–34
28. Y.M. Wang, X. Xiong, Z.W. Zhao, X. Lu, J.H. Yan, X.B. Min and F. Zheng, Near-net-shape Tungsten-rhenium Alloy Parts Produced by Plasma Spray Forming and Hot Isostatic Pressing, *Mater. Trans.*, 2014, **55**, p 713–721
29. S. Pramanik, A. K. Srivastav, B. Manuel Jolly, N. Chawake, and B. S. Murty, Effect of Re on Microstructural Evolution and Densification Kinetics During Spark Plasma Sintering of Nanocrystalline W, *Adv. Powder Technol.*, 2019, **30**, p 2779-2786
30. C.F. Lo, P. Mcdonald, D. Draper and P. Gilman, Influence of Tungsten Sputtering Target Density on Physical Vapor Deposition Thin Film Properties, *J. Electron. Mater.*, 2005, **34**, p 1468–1473
31. T. Leonhardt, C. Trybus and R. Hickman, Consolidation Methods for Spherical Rhenium and Rhenium Alloys, *Powder Metall.*, 2003, **46**, p 148–153

32. R.I. Jaffee, C.T. Sims, and J. J. Hardwood, The Effect of Rhenium on the Fabrication and Ductility of Molybdenum and Tungsten, In *Proceedings of 3rd Plansee-Seminar Proceedings* (Reutte, Austria: Plansee Group), 1958, p 380-410
33. K. Johann, L. Alexander, K. Daniel, C. Helmut, and M.K. Verena, Thermally Activated Deformation Mechanisms and Solid Solution Softening in W-Re Alloys Investigated via High Temperature Nanoindentation, *Mater. Design*, 2020, **189**, p (108499)1-6
34. H. Wang, M.X. Xia, Y.C. Li, X.F. Liu, X.M. Cai, R. Bai and X. Zhang, Treatment of Ammonia Nitrogen Waste Water from Tungsten Smelter by Breakpoint Chlorination, *Chin. Tungsten Indus.*, 2019, **34**, p 64–69
35. Z.J. Liu, Y.X. Chen, W.J. Huang and H.J. Huang, Manufacture and Application of Sputtering Target Materials, *South. Metal.*, 2003, **23**, p 23–25
36. Q. Tan, Manufacture and Application of Mo-Re Alloys, *Chin. Molybden. Indus.*, 1998, **22**, p 26–28
37. X.S. Yin, *Tungsten/Rhenium Alloy and Tungsten/Rhenium Thermocouple*, Metall. Indus. Press, Beijing, 1992, p 7
38. C. Guan, J.J. He, H. Zeng, X.Y. Wang and Y.J. Li, Microstructure and Texture Evolution of Ultra-high Pure CuMn Alloy Material, *Chin. Rare Metal.*, 2017, **41**, p 120–125
39. C.B. Wei, M.J. Dai, H.J. Hou, S.S. Lin and L. Zhao, Influence of Deposition Pressure on Structure and Tribological Properties of W-S-C Composite Films, *Lubr. Eng.*, 2012, **37**, p 69–73
40. J.T. He, H.C. Cai and Y.J. Xue, Effect of Deposition Pressure on Tribological Properties of WS_2 Films by Magnetron Sputtering, *Surf. Technol.*, 2020, **49**, p 180–187